GEOPHYSICS

Gravitational collapse of Mount Etna's southeastern flank

Morelia Urlaub[1]*, Florian Petersen[1], Felix Gross[2], Alessandro Bonforte[3], Giuseppe Puglisi[3], Francesco Guglielmino[3], Sebastian Krastel[2], Dietrich Lange[1], Heidrun Kopp[1,2]

The southeastern flank of Etna volcano slides into the Ionian Sea at rates of centimeters per year. The prevailing understanding is that pressurization of the magmatic system, and not gravitational forces, controls flank movement, although this has also been proposed. So far, it has not been possible to separate between these processes, because no data on offshore deformation were available until we conducted the first long-term seafloor displacement monitoring campaign from April 2016 until July 2017. Unprecedented seafloor geodetic data reveal a >4-cm slip along the offshore extension of a fault related to flank kinematics during one 8-day-long event in May 2017, while displacement on land peaked at ~4 cm at the coast. As deformation increases away from the magmatic system, the bulk of Mount Etna's present continuous deformation must be driven by gravity while being further destabilized by magma dynamics. We cannot exclude flank movement to evolve into catastrophic collapse, implying that Etna's flank movement poses a much greater hazard than previously thought. The hazard of flank collapse might be underestimated at other coastal and ocean island volcanoes, where the dynamics of submerged flanks are unknown.

INTRODUCTION

Volcanic flanks can slide in response to various internal and external forces. For example, the unbalanced weight distribution of a volcanic edifice and horizontal "pushing" due to magmatic intrusions can trigger flank spreading. Unstable flanks can fail catastrophically and result in giant landslides, such as those at the submarine slopes off Hawaii (*1*–*3*). Catastrophic collapses of ocean island volcanoes or those built at the shoreline pose the largest threat as the sudden displacement of large amounts of material in water can trigger tsunamis with extreme effects (*4*, *5*). Assessing the hazard potential of catastrophic collapse requires a profound understanding of the mechanisms that cause flank movement, which is also crucial for the design of appropriate monitoring strategies.

Numerous hypotheses have been proposed to explain flank sliding at Mount Etna, including increases in magma pressure (*6*), eruptive activity (*7*), repeated dyke intrusions (*8*), basement uplift (*9*), gravitational spreading (*10*), gravitational reorganization (*11*), gravity-driven instability accelerated by inflation and/or lateral intrusions (*12*), or combined magmatic inflation and continental margin instability (*13*). All hypotheses are derivatives of two basic processes capable of triggering flank instability: horizontal pushing of ascending magmatic intrusions or gravitational pull. These end-member mechanisms have fundamentally different hazard implications: While magma dynamics can trigger slope failures near the magma pathways (*14*), gradual deep-seated gravitational deformation can induce catastrophic collapse as in the cases of Mombacho (*15*), Kilauea (*2*), other Hawaiian volcanoes (*3*), and Ritter Island, Papua New Guinea (*16*). The overall consensus for Etna has been that it is mainly the magnetic plumbing system that drives movement of the unstable southeastern flank, rather than gravitational or tectonic forces.

Uncertainties regarding the causes of flank sliding originate from the lack of information on the dynamics of the submarine part of Etna volcano. Onshore geodetic measurements have documented large-scale continuous seaward motion at an average rate of 3 to 5 cm per year since the early 1980s (*8*, *10*, *17*, *18*), immediately evidencing the highest rates at the coast (*19*, *20*). However, no information on the movement of the submarine part of the flank existed before this study. Here, we document rapid deformation of Etna's offshore flank and combine the offshore measurements with onshore ground deformation. Our combined onshore-offshore data define the dynamics of the entire volcanic flank.

Seafloor displacement measurements at Etna's submerged flank

Established satellite-based geodetic tools are not adaptable for use in the marine environment due to the opacity of seawater to electromagnetic waves. Underwater, distances can be estimated with the sound speed of water and travel time measurements between transponders on the seafloor. Periodic back-and-forth acoustic interrogations between several transponders equipped with absolute pressure sensors and arranged in a network allow continuous determination of seafloor displacement in horizontal and vertical directions within the network (*21*–*23*). A network of five such transponders was placed on both sides of the submerged southern boundary of Etna's unstable flank (*24*) at a water depth of ~1200 m. Changes in distance between transponders across the fault and increases in pressure at transponders to the north of the fault indicate movement of the presumed unstable flank relative to the stable surrounding. Our seafloor network is the first to monitor an offshore strike-slip event in subcentimeter resolution, therewith proving the feasibility of the emerging acoustic direct-path ranging method to monitor volcanic flank instability.

On land, the spatial outline of the unstable flank is well defined by geodetic, geophysical, and geological methods (Fig. 1): Along the northern boundary of the unstable flank, deformation focuses along the left-lateral Pernicana fault (*17*). To the south, the right-lateral Tremestieri and Acitrezza (ATF) fault systems accommodate most of the flank movement (*17*, *25*). Off the coast, the Riposto Ridge forms the prolongation of the northern boundary. In distal direction,

[1]GEOMAR Helmholtz Centre for Ocean Research Kiel, 24148 Kiel, Germany. [2]Institute of Geosciences, Kiel University, 24118 Kiel, Germany. [3]Istituto Nazionale di Geofisica e Vulcanologia, Sezione di Catania, Osservatorio Etneo, Catania 95125, Italy.
*Corresponding author. Email: murlaub@geomar.de

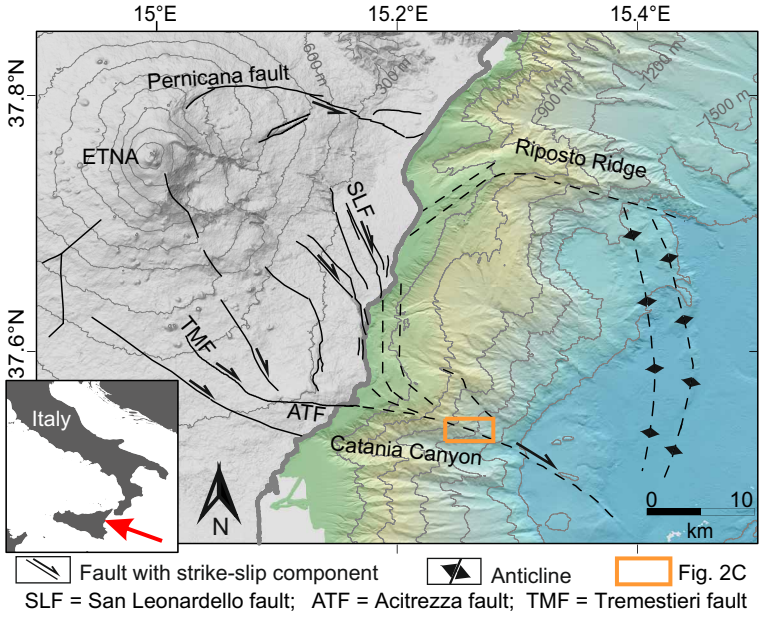

Fig. 1. Morphologic map of Mount Etna including tectonic features of the southeastern flank. Onshore topography in gray and offshore bathymetry in green to blue colors. Contour line interval is 300 m. Main features are shown as dashed (*24*) and solid (*38*) black lines. The thick gray line delineates the coastline. The orange rectangle marks the location of the seafloor geodetic network.

two anticlines observed in seismic reflection data mark the seaward termination of the unstable volcanic flank (Fig. 1) (*24*). To the south, a right-lateral transpressive fault north of Catania Canyon, interpreted as the offshore prolongation of onshore fault systems, represents the southern boundary of the unstable flank (*13*, *24*).

This fault is a pronounced west-east striking feature in the bathymetry (Figs. 1 and 2C). Seismic data indicate distinct reflection characteristics on either side of the fault (fig. S1) (*24*). On the basis of these observations, we deployed transponders 1 and 4 south of the fault and transponders 2, 3, and 5 north of the fault (Fig. 2C). All transponders were in line of sight of each other, resulting in 10 baselines with distances between 144 and 1254 m. All transponders monitored distances to all other transponders and pressures every 90 min. Periodic data upload via an acoustic link provided a continuous time series from April 2016 to July 2017.

RESULTS

For most parts of the observation period, acoustic distances between transponders remained stable within approximately 0.5 cm (Fig. 2 and fig. S2). However, a significant change in distances occurred between 12 and 20 May 2017. Only baselines across the fault recorded the 8-day-long aseismic fault motion that stands out from the background noise (Fig. 2 and fig. S2). Relative distance changes during the May 2017 event ranged between 0.6 and −3.9 cm for different transponder pairs (Table 1, Fig. 2, and fig. S2). As expected for a dextral strike-slip fault, length changes are dependent on the angle of the baseline to the fault (fig. S3). This angle can be used to determine true fault slip. The main uncertainty in slip results from the lack of knowledge of the exact fault trace on the seafloor. The ranging data confirm that the fault trace must run in the very narrow corridor between transponders 1 and 3 (Fig. 2C) within a range of 5°. Taking into account all fault crossing baselines, the true slip is between 3.87 and 4.23 cm (Table 1). We also observe that transponders on the north side of the fault showed a downward vertical displacement of 1 cm relative to those on the south side during the May 2017 event (Fig. 2 and fig. S4).

Overall, no significant changes in distances or depths occurred between transponders that were located on the same fault side (Fig. 2 and figs. S2 to S4). We exclude the possibility of a local landslide coherently moving these transponders based on the lack of evidence for soft sediments in seismic and sediment echosounder data, as well as in seafloor samples. The observed distance changes are in all aspects consistent with right-lateral strike-slip movement separating transponders 2, 3, and 5 from transponders 1 and 4 (Fig. 2C).

Notably, the observed length change in the network of ~4 cm provides a minimum estimate of the true slip along the fault during the May 2017 event. The gross motion of the unstable flank might not have been fully captured, leading to a potential underestimation of slip. The southern boundary fault splits into several branches toward the seafloor, as imaged in seismic data (fig. S1) (*24*). The network of transponders, however, does not span over all fault branches. Branches out of the reach of our network may have also accommodated flank movement during the investigated time period.

A slip of 4 cm corresponds to a moment magnitude release equivalent to a M_w of 4.3 to 5.3 earthquake (*26*). Since the initiation of instrumental seismic recording at Etna in the 1980s, no earthquake with a magnitude larger than 4 has been observed in the area (*27*). Hence, the main style of deformation of the offshore volcanic flank is episodic and aseismic sliding rather than seismic rupture.

Overall flank dynamics

Our offshore observations show that the submarine part of Mount Etna's southeastern flank moves in east and downward direction with a minimum aseismic fault slip of at least 4 and 1 cm relative subsidence, respectively (Fig. 2). The total slip may be even larger as

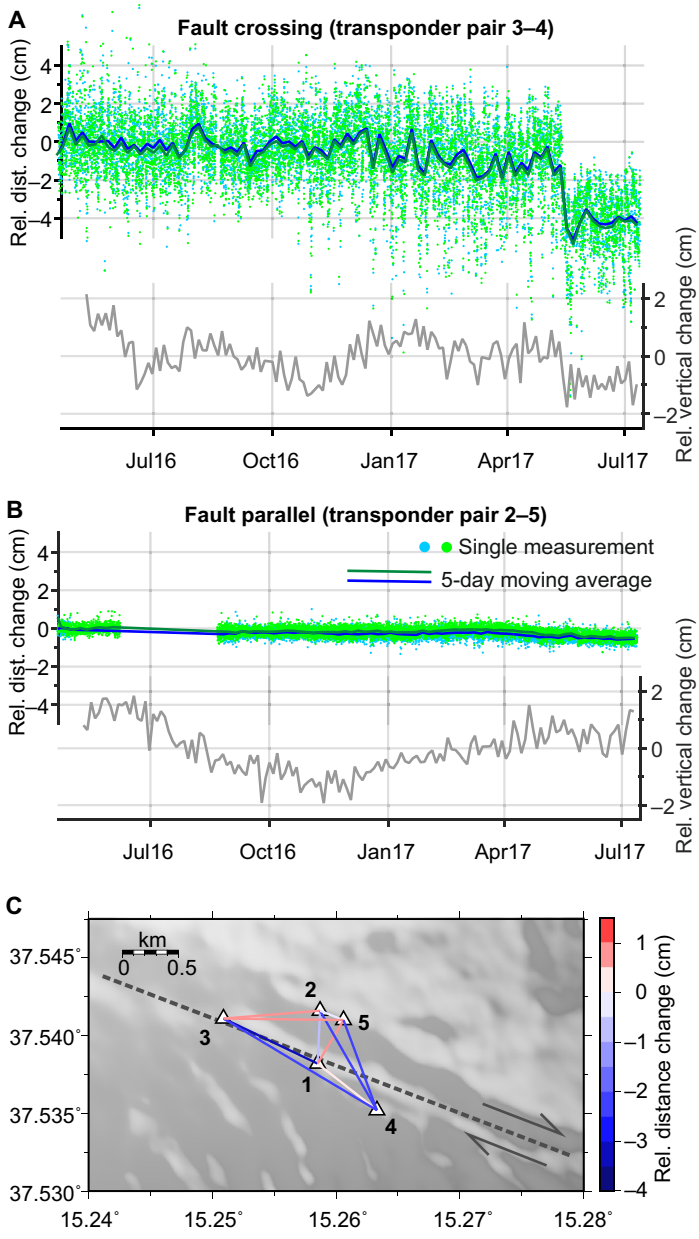

Fig. 2. Seafloor deformation across the fault that marks the offshore southern boundary of Mount Etna's unstable flank, as recorded by the network of five autonomous monitoring transponders. (**A** and **B**) Relative changes in distances between transponder pairs (blue and green colors indicate active interrogation and passive response of acoustic signals, respectively) and relative vertical displacement between transponder pairs (gray line, 3-day moving average). Time series for all other transponder pairs are shown in figs. S2 and S3. (**C**) Map view of relative distance changes within the array during the observation period plotted on gray-shaded bathymetry (see Fig. 1 for location). Black numbers indicate transponder numbers.

not all fault branches could be captured by the seafloor network (fig. S1). Onshore, the seaward flank motion at Etna in the observation period April 2016 to July 2017 manifested in continuous deformation (fig. S8) rather than in episodic slip, as observed offshore. Cumulative displacements were highest along the coast (Fig. 3). SISTEM (simultaneous and integrated strain tensor estimation from geodetic and satellite deformation measurements) integration of GPS (fig. S5) and DInSAR (Differential Interferometry Synthetic Aperture Radar) (fig. S6) data (*28*) shows that flank movement mainly occurred across the ATF and San Leonardello fault (Fig. 3 and fig. S7) with a maximum slip of ~2 cm along each fault. The offshore flank movement was thus in the same order of magnitude as the sum of onshore fault slips for identical periods of time. Therefore, the offshore fault probably cumulated the slip of both the ATF and San Leonardello fault.

Gross onshore and offshore movements are kinematically consistent (Fig. 4) and, therefore, are expressions of the same underlying process related to flank instability. The observed differences in fault slip mode during the observation period, i.e., continuous creep onshore and slow slip offshore, can result from variations in fault properties, such as temperature, fluid pressure, or fault gouge material

Table 1. Characteristics of the May 2017 event for all fault crossing baselines. The 1 − σ value is based on the pre-event signal. Fault slip is calculated for three possible fault traces and the corresponding angle α of the baselines to the fault. The resulting mean slip from all baselines is 3.93 cm.

Crossing baseline	Baseline length	Length change	1 − σ	α_1	α_2	α_{mean}	$Slip_1$	$Slip_2$	Mean slip
	(m)	(cm)	(cm)	(°)	(°)	(°)	(cm)	(cm)	(cm)
1–2	368.357	−1.09	0.55	67.2	72.2	69.7	2.82	3.57	3.15
2–4	804.192	−3.32	0.83	34.4	39.4	36.9	4.02	4.30	4.15
4–5	688.623	−2.88	0.66	43.6	48.6	46.1	3.98	4.36	4.16
1–5	350.719	0.62	0.51	94.9	99.9	97.4	7.22	3.59	4.79
3–4	1253.642	−3.46	1.54	5.5	10.5	8.0	3.47	3.51	3.49
1–3	699.045	−3.86	1.61	0.5	5.5	3.0	3.86	3.87	3.86
						Mean slip:	**4.23**	**3.87**	**3.93**

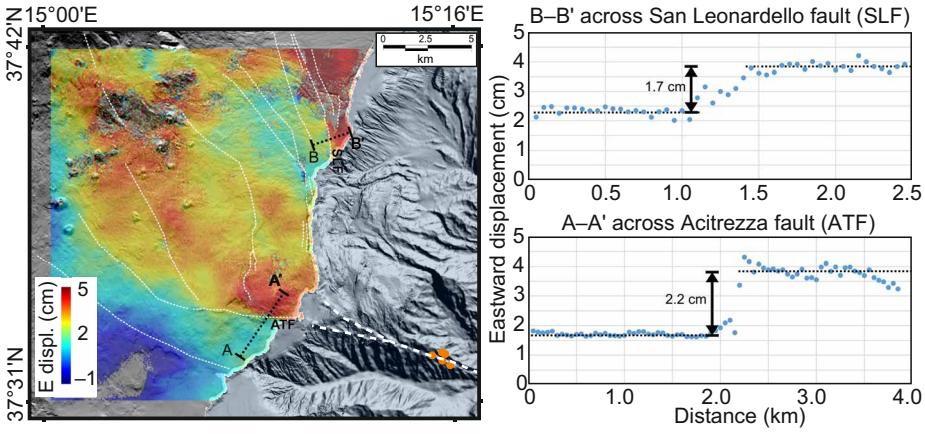

Fig. 3. Eastward displacement of the southeastern flank of Mount Etna from April 2016 to July 2017. The map is obtained by integrating GPS and InSAR analysis using the SISTEM method (*28*). White dashed lines show principal faults. Dots show locations of the seafloor geodetic transponders.

(*29*), while still representing the same overall dynamics. Nevertheless, onshore deformation at Etna's unstable flank also manifests in slow slip events along the coastline, as monitored by continuous GPS (*8*).

DISCUSSION

Reasons for instability of Mount Etna's southeastern flank have been related either to the volcano's magmatic plumbing system or to gravitational forces. Displacement induced by magma injection strongly decays with distance to the dyke (*30*). Inflation of the volcanic edifice caused by uprising magma is expected to cause the highest displacements near the volcanic center, which is inconsistent with our data. In contrast, our geodetic measurements demonstrated that flank movement increases away from the summit toward the coast and into the Ionian Sea, while no increase in magma activity was noticed simultaneous to the May 2017 offshore event, implying that magma dynamics cannot be solely responsible for the observed deformation pattern. The comparison of onshore and offshore fault slip further suggests that offshore deformation focuses along one fault north of Catania Canyon and that strain is partitioned near the coast into two fault systems (Fig. 4). The observations of (i) largest deformation away from and (ii) strain partitioning toward the summit indicate that the basal shear zone accommodating flank movement began offshore and has developed retrogressively landward. Therefore, the forcing mechanism that controls the bulk of Mount Etna's flank movement must have its origin seaward and is separated from the volcanic edifice. Gravitational pull of the subsiding continental margin is a potential tectonic trigger (*17*).

Yet, magmatic activity also influences flank movement as episodic accelerations of onshore flank movement have been related to dyke intrusions and magma ascent repeatedly (*8*, *25*). Analyses of onshore seismic and ground deformation data show a clear decoupling of the shallow and deep strain regimes beneath the eastern flank at a depth of 2 km during an inflation period (*31*). Inflation and dyke intrusions can thus favor episodic accelerations of flank movement in addition to large-scale continuous gravitational sliding. Both processes may well interact with and influence each other, as demonstrated by analog models (*32*).

Marine geological records off the Canary Islands document that large-scale submarine flank failures occurred in multiple stages, all preceding explosive eruptions (*33*). A similar pattern is recorded in sediment cores at Etna's submerged flank, where ash layers overlie landslide deposits (*34*). These observations further support a close interaction of flank movement and magmatic activity. However, eruptions do not trigger catastrophic flank collapses, implying that gravitational sliding is the governing process.

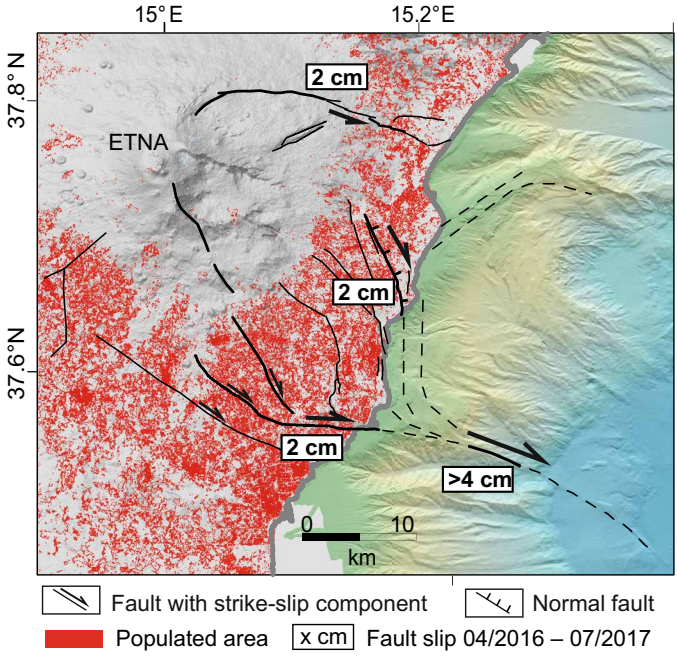

Fig. 4. Shoreline-crossing fault slip representation of Mount Etna's southeastern flank movement. Populated areas are obtained from a Landsat-8 classification on a 30 m by 30 m grid (Landsat-8 image courtesy of the U.S. Geological Survey). Bold lines represent main active features during the observation period.

Our results show that only the combination of onshore and offshore ground deformation data gives a clear picture of overall volcano flank dynamics, from which the hazard of catastrophic flank collapse can be assessed. In the case of Mount Etna, our shoreline-crossing deformation analysis implies a greater hazard for flank collapse than previously assumed, as deep-seated gravitational sliding can potentially lead to catastrophic collapse (*2*, *3*, *16*). Onshore ground deformation analyses reveal signs of ongoing flank instability at numerous coastal and ocean island volcanoes today (*35*). Volcanoes, including those in Hawaii, the Canary Islands, and La Réunion, are potentially liable to collapse, but shoreline-crossing ground deformation analyses are needed to obtain a comprehensive view of the dynamics and constrain the hazard. Our results demonstrate both that seafloor geodetic investigations are capable of characterizing the dynamics of submerged volcanic flanks and that such investigations provide deformation data at a resolution comparable to GPS.

MATERIALS AND METHODS

Bathymetry

Bathymetric data were acquired during research vessel (RV) *Meteor* expedition M86/2 in 2012 with hull-mounted Kongsberg Simrad EM122 and EM710 multibeam sounders. Standard data processing with MB-System produced a grid with a cell size of 30 m by 30 m. Coastal bathymetry was acquired in the framework of the MaGIC (Marine Geohazards along the Italian Coast) project (*36*).

Seafloor geodesy

The direct-path acoustic ranging method provides relative positioning by using high-precision acoustic transponders [Sonardyne Autonomous Monitoring Transponders (AMT)]. Multiple transponders installed at the seafloor measure the time of flight of acoustic signals between them with a microsecond resolution and water sound speed, temperature, and absolute pressure. Travel time observations were converted into distances with millimetric precision. Pressure measurements provided information on vertical displacement. Dual-axis inclinometers detected changes in instrument tilt. Repeated interrogations over months to years allowed the determination of displacements and, hence, deformation of the seafloor inside the network for extended periods, depending on battery capacity.

Here, we used five transponders from GEOMAR's GeoSEA array. The transponders communicated with 8-ms phase-codes pulses and an 8-kHz bandwidth with a centered frequency of 18 kHz. The acoustic ranges were calculated by cross-correlation of the interrogation and receiving signals. The AMTs logged pressure, temperature, tilt, and sound speed. The log period for each transponder was set to 90 min. We noted instability in the sound speed measurement and recalculated the sound speed using the high-resolution temperature and pressure measurements at each transponder and assuming a constant salinity of 34 practical salinity units (*37*). We removed the tide signals from the pressure data using the data provided by the Istituto Superiore per la Protezione e la Ricerca Ambientale tide gauge in the port of Catania (www.mareografico.it). Pressure was converted to depth with the seawater density of 1024 kg/m^3. For better comparison to the relative distance measurements obtained by acoustic telemetry, and because we are mostly interested in the relative movement of the unstable sector compared to the stable sector, we only showed relative vertical displacement between transponder pairs. These were obtained by subtracting the time series recorded by one transponder from that of another transponder.

The autonomous monitoring transponders were located at the outcrop of a fault at the seafloor. Locations for individual transponders were chosen on the basis of a closely spaced high-resolution two-dimensional (2D) seismic survey and swath bathymetric data. The network design ensures that at least two AMTs sit at each side of the fault and are in acoustic sight of each other. The AMTs were mounted on anchored buoyancy bodies. The deployed trapeze-shaped setup results in 10 monitored baselines. Besides transponder 1, all baselines were recorded in two directions (forward and backward measurements), resulting in six bidirectional baselines and four unidirectional baselines. Distances for forward (for example, measuring the travel time from AMT 1 to 2 and return) and backward measurements (measuring from AMT 2 to 1 and return) closely agree for all transponder pairs.

We deployed the transponders in April 2016 during RV *Poseidon* expedition *POS496* at meter precision using ultrashort baseline acoustic positioning in water depths of 950 to 1180 m. Data stored in each station were uploaded from the seafloor to the surface with an acoustic modem.

Onshore geodesy

We processed and integrated the onshore data covering the same period as the offshore data acquisitions to compare the results and extend the information about the deformation measured by the seafloor network. GPS data collected during the first week of April 2016 and the last week of July 2017 were processed separately by using the usual approach adopted for geodetic surveys (*38*) to obtain the most precise coordinates of each station at the two periods. Thus, the 3D displacements at the GPS stations from April 2016 to July 2017 were obtained by comparing the two sets of coordinates.

The Sentinel-1A ascending (31 March 2016 and 30 July 2017) and descending (6 April 2016 and 30 July 2017) data were processed by GAMMA software, using the so-called two-pass interferometry (*39*) to generate the interferometric products. A spectral diversity method was used to coregister the Sentinel-1 pairs to obtain an extremely high precision (<0.01 pixel). The result of this processing is the ground displacement along the Line Of Sight (LOS) across the entire area. To derive the 3D surface motion maps, we integrated GPS and DInSAR displacements by applying the SISTEM method (*28*). A linear matrix equation accounts for both GPS and DInSAR data, the solution of which provides the strain tensor, the displacement field, and the rigid body rotation tensor throughout the entire investigated area.

SUPPLEMENTARY MATERIALS

Supplementary material for this article is available at http://advances.sciencemag.org/cgi/content/full/4/10/eaat9700/DC1

Supplementary Text

Fig. S1. Close-up bathymetric map and seismic image of the area with the seafloor geodetic network.

Fig. S2. Relative changes in distances for all 10 baselines during the entire observation period from April 2016 to July 2017.

Fig. S3. Cosine relationship between the relative distance shortening and lengthening during the May 2017 event and the angle at which the baselines cut the fault trace.

Fig. S4. Relative pressure differences for the entire observation period (10-day moving average) between individual transponder pairs.

Fig. S5. GPS displacements referring to the April 2016 to July 2017 comparison.

Fig. S6. Ascending 31 March 2016 to 30 July 2017 and descending 6 April 2016 to 30 July 2017 Sentinel-1 phase interferograms.

Fig. S7. East, north, and up displacement components resulting from the SISTEM integration.

Fig. S8. Ground displacements along the LOS across the study area measured by both Sentinel 1A and 1B satellites with a 6-day interval.

Reference (*40*)

REFERENCES AND NOTES

1. J. G. Moore, D. A. Clague, R. T. Holcomb, P. W. Lipman, W. R. Normark, M. E. Torresan, Prodigious submarine landslides on the Hawaiian Ridge. *J. Geophys. Res.* **94**, 17465–17484 (1989).
2. J. K. Morgan, G. F. Moore, D. J. Hills, S. Leslie, Overthrusting and sediment accretion along Kilauea's mobile south flank, Hawaii: Evidence for volcanic spreading from marine seismic reflection data. *Geology* **28**, 667–670 (2000).
3. R. P. Denlinger, J. K. Morgan, Instability of Hawaiian volcanoes, in *Characteristics of Hawaiian Volcanoes*, M. P. Poland, T. J. Takahashi, C. M. Landowski, Eds. (Professional Paper 1801, U.S. Geological Survey, 2014).
4. B. H. Keating, W. J. McGuire, Island edifice failures and associated tsunami hazards. *Pure Appl. Geophys.* **157**, 899–955 (2000).
5. R. S. Ramalho, G. Winckler, J. Madeira, G. R. Helffrich, A. Hipólito, R. Quartau, K. Adena, J. M. Schaefer, Hazard potential of volcanic flank collapses raised by new megatsunami evidence. *Sci. Adv.* **1**, e1500456 (2015).
6. P. Lundgren, F. Casu, M. Manzo, A. Pepe, P. Berardino, E. Sansosti, R. Lanari, Gravity and magma induced spreading of Mount Etna volcano revealed by satellite radar interferometry. *Geophys. Res. Lett.* **31**, L04602 (2004).
7. V. Acocella, B. Behncke, M. Neri, S. D'Amico, Link between major flank slip and 2002–2003 eruption at Mt. Etna (Italy). *Geophys. Res. Lett.* **30**, 2286 (2003).
8. V. Bruno, M. Mattia, E. Montgomery-Brown, M. Rossi, D. Scandura, Inflation leading to a Slow Slip Event and volcanic unrest at Mt. Etna in 2016: Insights from CGPS data. *Geophys. Res. Lett.* **44**, 12141–12149 (2017).
9. I. Stewart, W. J. McGuire, C. Vita-Finzi, C. Firth, R. Holmes, S. Saunders, Active faulting and neotectonic deformation on the eastern flank of Mount Etna, Sicily. *Zeits. Geomorph.* **94**, 73–94 (1993).
10. A. Borgia, L. Ferrari, G. Pasquarè, Importance of gravitational spreading in the tectonic and volcanic evolution of Mount Etna. *Nature* **357**, 231–235 (1992).
11. O. Merle, A. Borgia, Scaled experiments of volcanic spreading. *J. Geophys. Res.* **101**, 13805–13817 (1996).
12. A. Bonforte, A. Bonaccorso, F. Guglielmino, M. Palano, G. Puglisi, Feeding system and magma storage beneath Mt. Etna as revealed by recent inflation/deflation cycles. *J. Geophys. Res.* **113**, B05406 (2008).
13. F. L. Chiocci, M. Coltelli, A. Bosman, D. Cavallaro, Continental margin large-scale instability controlling the flank sliding of Etna volcano. *Earth Planet Sci. Lett.* **305**, 57–64 (2011).
14. A. Bonforte, F. Guglielmino, Very shallow dyke intrusion and potential slope failure imaged by ground deformation: The 28 December 2014 eruption on Mount Etna. *Geophys. Res. Lett.* **42**, 2727–2733 (2015).
15. B. van Wyk de Vries, P. W. Francis, Catastrophic collapse at stratovolcanoes induced by gradual volcano spreading. *Nature* **387**, 387–390 (1997).
16. J. Karstens, M. Urlaub, C. Berndt, S. F. L. Watt, A. Micaleff, I. Klaucke, D. Klaeschen, S. Brune, M. Kühn, The complex emplacement dynamics and tsunami genesis of the 1888 Ritter Island sector collapse from 3D seismic data, paper presented at the AGU Fall Meeting, New Orleans, LA, 11 to 15 December 2017.
17. A. Bonforte, F. Guglielmino, M. Coltelli, A. Ferretti, G. Puglisi, Structural assessment of Mount Etna volcano from permanent scatterers analysis. *Geochem. Geophys. Geosyst.* **12**, Q02002 (2011).
18. D. Patanè, P. De Gori, C. Chiarabba, A. Bonaccorso, Magma ascent and the pressurization of Mount Etna's volcanic system. *Science* **299**, 2061–2063 (2003).
19. G. Puglisi, A. Bonforte, Dynamics of Mount Etna Volcano inferred from static and kinematic GPS measurements. *J. Geophys. Res.* **109**, B11404 (2004).
20. N. Houlié, P. Briole, A. Bonforte, G. Puglisi, Large scale ground deformation of Etna observed by GPS between 1994 and 2001. *Geophys. Res. Lett* **33**, L02309 (2006).
21. J. J. McGuire, J. A. Collins, Millimeter-level precision in a seafloor geodesy experiment at the discovery transform fault, East Pacific Rise. *Geochem. Geophys. Geosyst.* **14**, 4392–4402 (2013).
22. R. Bürgmann, D. Chadwell, Seafloor geodesy. *Annu. Rev. Earth Planet Sci.* **42**, 509–534 (2014).
23. B. A. Brooks, J. H. Foster, J. J. McGuire, M. Behn, Submarine landslides and slow earthquakes: Monitoring motion with GPS and seafloor geodesy, in *Encyclopedia of Complexity and System Science*, W. Lee, Ed. (Springer, 2011), pp. 889–907.
24. F. Gross, S. Krastel, J. Geersen, J. H. Behrmann, D. Ridente, F. L. Chiocci, J. Bialas, C. Papenberg, D. Cukur, M. Urlaub, A. Micallef, The limits of seaward spreading and slope instability at the continental margin offshore Mt Etna, imaged by high resolution 2D seismic data. *Tectonophysics* **667**, 63–76 (2016).
25. A. Bonforte, F. Guglielmino, G. Puglisi, Interaction between magma intrusion and flank dynamics at Mt. Etna in 2008, imaged by integrated dense GPS and DInSAR data. *Geochem. Geophys. Geosyst.* **14**, 2818–2835 (2013).
26. T. C. Hanks, H. Kanamori, H. A. Moment Magnitude Scale. *J. Geophys. Res.* **84**, 2348–2350 (1979).
27. S. Alparone, A. Bonaccorso, A. Bonforte, G. Currenti, Long-term stress-strain analysis of volcano flank instability: The eastern sector of Etna from 1980 to 2012. *J. Geophys. Res.* **18**, 5098–5108 (2013).
28. F. Guglielmino, C. Bignami, A. Bonforte, P. Briole, F. Obrizzo, G. Puglisi, S. Stramondo, U. Wegmüller, Analysis of satellite and in situ ground deformation data integrated by the SISTEM approach: The April 3, 2010 earthquake along the Pernicana fault (Mt. Etna - Italy) case study. *Earth Planet. Sci. Lett.* **312**, 327–336 (2011).
29. C.H. Scholz, *The Mechanics of Earthquakes and Faulting* (Cambridge Univ. Press, 2002).
30. D. Elsworth, B. Voight, Dike intrusion as a trigger for large earthquakes and the failure of volcano flanks. *J. Geophys. Res.* **100**, 6005–6024 (1995).
31. S. Alparone, G. Barberi, A. Bonforte, V. Maiolino, A. Ursino, Evidence of multiple strain fields beneath the eastern flank of Mt. Etna volcano (Sicily, Italy) deduced from seismic and geodetic data during 2003–2004. *Bull. Volcanol.* **73**, 869–885 (2011).
32. N. Le Corvec, T. R. Walter, J. Ruch, A. Bonforte, G. Puglisi, Experimental study of the interplay between magmatic rift intrusion and flank instability with application to the 2001 Mount Etna eruption. *J. Geophys. Res.* **119**, 5356–5368 (2014).
33. J. Hunt, M. Cassidy, P. J. Talling, Multi-stage volcanic island flank collapses with coeval explosive caldera-forming eruptions. *Sci. Rep.* **8**, 1146 (2018).
34. F. Gross, S. Krastel, F. L. Chiocci, D. Ridente, J. Bialas, J. Schwab, J. Beier, D. Cukur, D. Winkelmann, Evidence for Submarine Landslides Offshore Mt. Etna, Italy, in *6th International Symposium. Submarine Mass Movements and Their Consequences. Advances in Natural and Technological Hazards Research*, S. Krastel, J.-H. Behrmann, D. Völker, M. Stipp, C. Berndt, R. Urgeles, J. Chaytor, K. Huhn, M. Strasser, C. B. Harbitz, Eds. (Springer, 2014), vol. 37, pp. 307–316.
35. M. P. Poland, A. Peltier, A. Bonforte, G. Puglisi, The spectrum of persistent volcanic flank instability: A review and proposed framework based on Kīlauea, Piton de la Fournaise, and Etna. *J. Volcanol. Geotherm. Res.* **339**, 63–80 (2017).
36. F. L. Chiocci, D. Ridente, Regional-scale seafloor mapping and geohazard assessment. The experience from the Italian project MaGIC (Marine Geohazards along the Italian Coasts). *Mar. Geophys. Res.* **32**, 13–23 (2011).
37. V. Leroy, A. Strybulevych, J. H. Page, M. G. Scanlon, Sound velocity and attenuation in bubbly gels measured by transmission experiments. *J. Acoust. Soc. Am.* **123**, 1931–1940 (2008).
38. G. Barreca, A. Bonforte, M. Neri, A pilot GIS database of active faults of Mt. Etna (Sicily): A tool for integrated hazard evaluation. *J. Volcanol. Geotherm. Res.* **251**, 170–186 (2013).
39. D. Massonnet, K. L. Feigl, Radar interferometry and its application to changes in the Earth's surface. *Rev. Geophys.* **36**, 441–500 (1998).

40. S. Ide, G. C. Beroza, D. R. Shelly, T. Uchide, A scaling law for slow earthquakes. *Nature* **447**, 76–79 (2007).

Acknowledgments: We thank the captains, crews, and scientific parties of the cruises *POS496*, *POS515*, and *Tethys-II* (CRACK) for deployment of seafloor instruments and recovery of the data set. We also thank the INGV researchers and technicians for maintaining the GPS monitoring network and data and C. Hammersley and T. Bennetts from Sonardyne for technical support related to the AMTs. We thank C. Berndt and J. Geersen for discussions. Seafloor geodetic stations were positioned using the procedure patented under DE 102016107558 A1 2017.10.26. **Funding:** The GeoSEA Array is funded through grant 03F0658I of the BMBF (German Federal Ministry of Education and Research). Part of this work was funded by grant CP1635 of the Cluster of Excellence 80 "The Future Ocean." The Future Ocean is funded within the framework of the Excellence Initiative by the Deutsche Forschungsgemeinschaft on behalf of the German federal and state governments. **Author contributions:** M.U., F. Gross, and G.P. were responsible for the conception of this study. H.K., D.L., M.U., and F.P. are responsible for the design of the seafloor network and formal data analysis. F.P., F. Gross, and S.K. participated in the acquisition of marine data. A.B., F. Guglielmino, and G.P. formally analyzed the onshore data. M.U., F.P., F. Gross, A.B., and G.P. interpreted the data. M.U. drafted and prepared the article, and all authors critically reviewed it. **Competing interests:** D.L., H.K., and F.P. are inventors on a patent related to this work (no. DE 10 2016 107 558.2, filed on 22 April 2016, published on 26 October 2017). All other authors declare that they have no competing interests. **Data and materials availability:** The seafloor geodetic data are archived in the World Data Center PANGAEA and can be accessed under doi.pangaea.de/10.1594/PANGAEA.893036. Copernicus Sentinel-1 data (2016–2017) are available at the Copernicus Open Access Hub (https://scihub.copernicus.eu). All data needed to evaluate the conclusions in the paper are present in the paper and/or the Supplementary Materials. Additional data related to this paper may be requested from the authors.

Submitted 23 April 2018
Accepted 6 September 2018
Published 10 October 2018
10.1126/sciadv.aat9700

Citation: M. Urlaub, F. Petersen, F. Gross, A. Bonforte, G. Puglisi, F. Guglielmino, S. Krastel, D. Lange, H. Kopp, Gravitational collapse of Mount Etna's southeastern flank. *Sci. Adv.* **4**, eaat9700 (2018).